

Molecular beam epitaxy growth of $\text{Mn}_{4-x}\text{Ni}_x\text{N}$ thin films on $\text{MgO}(001)$ substrates and their magnetic properties

Taro Komori^a, Akihito Anzai^a, Toshiki Gushi^{a,b}, Kaoru Toko^a, and Takashi Suemasu^{a,*}

^a*Institute of Applied Physics, Graduate School of Pure and Applied Sciences, University of Tsukuba, Tsukuba, Ibaraki 305-8573, Japan*

^b*University Grenoble Alpes, CEA, CNRS, INAC-Spintec, Grenoble 38000, France*

ABSTRACT

We grew $\text{Mn}_{4-x}\text{Ni}_x\text{N}$ epitaxial thin films on $\text{MgO}(001)$ by molecular beam epitaxy, as well as studied their crystalline qualities and magnetic properties. The films were decomposed into Ni_3N or Mn-Ni alloys when $x \geq 2$, as confirmed by X-ray diffraction and reflection high-energy electron diffraction, but this decomposition was mitigated by reducing the substrate growth temperature. The lattice constants decreased with increased Ni substitution except when the Mn ratio was high, while the crystal orientation tended to degrade. The magnetic properties were measured via vibrating sample magnetometer, and it was found that the saturation magnetization (M_S) and perpendicular magnetic anisotropy (PMA) diminished with a small amount of Ni substitution. Specifically, the M_S value was remarkably decreased from 86.3 ± 1.1 emu/cm³ (Mn_4N) to 19.0 ± 0.5 emu/cm³ ($\text{Mn}_{3.85}\text{Ni}_{0.25}\text{N}$), and the magnetic anisotropy constant was decreased from approximately 0.94 to 0.027 Merg/cm³, respectively. The PMA vanished with further Ni substitution. Ultimately, a small M_S and a PMA were simultaneously achieved with a small amount of Ni substitution. These properties support spin transfer torque, which can be applied to the emerging non-volatile memory devices using domain wall motion.

*Electronic mail: suemasu@bk.tsukuba.ac.jp

Keywords: A1.Crystal structure, A3.Molecular beam epitaxy, B1.Mn₄N, B1.Ni₄N,
B1.MgO, B2.Magnetic materials

1. Introduction

It is expected that non-volatile memory with high performance and reliability can be achieved via moving magnetic domain walls (DWs) in ferromagnetic nanowires using a pulsed current, such as that demonstrated in racetrack memory and DW-motion magnetic random-access memory devices [1,2]. In these DW-motion magnetic devices, a small saturation magnetization (M_s) value enables a higher DW mobility and a perpendicular magnetic anisotropy (PMA) is required to move the DW with a small threshold current and enable wall movement with spin orbit torque. Thus, materials with these properties have been explored [3,4]. The existence of a small M_s and high PMA has been reported in Mn_4N thin films grown on glass [5], Si(001) [6], 6H-SiC(0001) [7], MgO(001) [8-13], and SrTiO₃(001) [9,14] substrates. These striking features led to a DW velocity of approximately 10^3 m/s with a current density of 1.5×10^{12} A/m² in Mn_4N nanowires [15]. Figure 1 shows the antiperovskite structure of Mn_4N , where Mn atoms occupy the corner (I) and face-centered (II) sites and an N atom occupies the body-centered site. The magnetic moments of the Mn atoms in bulk Mn_4N were measured using neutron diffraction at 77 K to be $3.85 \mu_B$ at the I sites and $-0.90 \mu_B$ at the II sites, where μ_B is the Bohr magneton [16]. Note that in Mn_4N thin films, the presence of in-plane tensile strains of $c/a=0.99$ have been reported for many types of substrates [8-10,12-14], where a is the in-plane lattice constant and c is the perpendicular lattice constant. In the antiperovskite structure, the II sites can be further divided into IIA and IIB sites under the presence of an external magnetic field, as shown in Fig. 1. In recent years, antiperovskite nitrides such as Mn_4N and their mixed-crystal thin films have attracted attention. The growth of $Co_xMn_{4-x}N$ and $Fe_{4-x}Mn_xN$ thin films by molecular beam epitaxy (MBE) and the evaluation of these crystalline structures and magnetic properties have been reported [14,15]. In this work, we focused on $Mn_{4-x}Ni_xN$,

in which the Mn atoms in Mn_4N were partially substituted with Ni atoms. Because $\text{Ni}_4\text{N(I)}$ is a cubic crystal and exhibits ferromagnetism with $T_C = 121$ K; at room temperature (RT), Ni_4N is thought to instead adopt the $\text{Ni}_4\text{N(II)}$ structure, which is a tetragonal structure exhibiting paramagnetism [17-19]. The Ni nitrides are very unstable compared with fcc-Ni, and decompose easily under thermal impact, etc. However, the growth of Ni_4N thin films on $\text{SrTiO}_3(001)$ substrates have been achieved recently [20]. Because the M_S of mixed-crystal nitrides has been reported to accord with the ratio of the components in $\text{Fe}_{4-x}\text{Mn}_x\text{N}$ [13], $\text{Fe}_{4-x}\text{Ni}_x\text{N}$ [20], and $\text{Fe}_{4-x}\text{Co}_x\text{N}$ [21], we anticipate that ferromagnetic nitrides with smaller M_S values and measurable PMA can be achieved by partially substituting the Mn atoms in Mn_4N with Ni atoms. This portends that the efficiency of the spin transfer torque and spin orbit interaction in these films will be enhanced and the current-driven magnetization reversal will be highly supported. In this way, faster DW motion with a smaller current density will be enabled. Further, it has been reported that the magnetic properties and crystalline lattices of antiperovskite nitrides such as Mn_3XN ($X = \text{Cu, Ni, Ag, Zn, Ga, etc.}$) are dependent on the density of the valence electrons, and these crystals have been grown and evaluated in many ways [22-25]. In particular, the calculation and validation of antiferromagnetism in non-collinear magnetic moments of $(\text{Mn,Ni})_4\text{N}$, and the negative thermal expansion at the Néel temperature have been reported [25-28]. However, growth of epitaxial thin films by MBE has not been attempted and their magnetic properties are still undetermined. Herein, therefore, we grew $\text{Mn}_{4-x}\text{Ni}_x\text{N}$ ($x = 0, 0.1, 0.25, 0.5, 0.75, 1, 2, 3, 4$) epitaxial thin films on $\text{MgO}(001)$ substrates by MBE and studied their crystalline structures and magnetic properties.

2. Experimental

The 30 nm-thick $\text{Mn}_{4-x}\text{Ni}_x\text{N}$ ($x = 0, 0.1, 0.25, 0.5, 0.75, 1, 2, 3, 4$) thin films were grown on $\text{MgO}(001)$ single-crystal substrates by MBE using solid sources of Mn and Ni and radio-frequency N plasma. The deposition rates of Mn and Ni were independently calculated and controlled via the Knudsen cell temperature. Calculations were performed with the assumption that the deposition rate of each atom type remained unchanged even if they were deposited at the same time. Because the vapor pressures of Mn and Ni were sufficiently low under the substrate temperature (T_s) used during the growth process, re-evaporation from the substrate was negligible. Therefore, this assumption was considered reasonable. The T_s was set at 450 °C for $x \leq 2$, and was decreased to 150 °C for $x \geq 2$ to ensure crystalline quality. These values of T_s were chosen with reference to a previous report on the growth of Mn_4N and Ni_4N by MBE [13,20]. The conditions for the N plasma was chosen to ensure an intensity of the spectrometer (QE Pro; Ocean Optics Inc.) around 2,900 counts at a wavelength of 336 nm, while the radio-frequency power was 107–110 W. After growth, a capping layer of 3 nm-thick SiO_2 or Ta was sputtered on the $\text{Mn}_{4-x}\text{Ni}_x\text{N}$ thin film *in situ*. The crystalline quality of the samples was evaluated using reflection high-energy electron diffraction (RHEED), out-of-plane (ω - 2θ) X-ray diffraction (XRD; Smart-Lab, Rigaku Inc.), X-ray ω -scan rocking curves (RC) and in-plane (ϕ - $2\theta\chi$) XRD. A Cu-K α radiation source was used for the XRD and Ge(220) single crystals were set as a monochromator for the out-of-plane XRD and ω -RC. The lattice constants were calculated using the angles of the diffracted peaks acquired by XRD.

The magnetic properties were evaluated by a vibrating sample magnetometer (VSM) using 6 mm \times 6 mm samples at RT. Next, to calculate K_u and the effective magnetic anisotropy constant (K_u^{eff}) we used

$$K_u = K_u^{\text{eff}} + 2\pi M_S^2, \quad (6)$$

$$K_u^{\text{eff}} = \left(\int_0^{M_s} H dm \right)_{\text{easy}} - \left(\int_0^{M_s} H dm \right)_{\text{hard}}, \quad (7)$$

where “easy” and “hard” indicate the magnetic easy and hard axes, respectively; and $2\pi M_s^2$ is the demagnetizing energy. In this experiment, we performed the integral calculation using the origin6.0j software after pursuing interpolation. When the magnetization in the hard axis did not saturate, we performed the integral calculation after pursuing extrapolation with the origin6.0j software.

3. Results and discussion

Figure 2 shows the out-of-plane XRD and RHEED patterns of 30 nm-thick $\text{Mn}_{4-x}\text{Ni}_x\text{N}$ ($x = 0, 0.1, 0.25, 0.5, 0.75, 1, 2, 3, 4$) films, and Fig. 3 shows the in-plane XRD patterns of these samples. The $\text{Mn}_{4-x}\text{Ni}_x\text{N}$ samples with $x = 0, 1$, which were grown at $T_S = 450$ °C, exhibit only c -axis-oriented XRD peaks and streaky RHEED patterns (Figs. 2 and 3), indicating epitaxial growth of these samples. Conversely, the XRD pattern of $x = 2$ exhibits diffraction peaks at $2\theta = 44.8^\circ$ and 50.32° instead of the peak of $\text{Mn}_2\text{Ni}_2\text{N}$ 002 diffraction (angles are from in-plane XRD). It is known that the 033 diffraction peak of α -Mn is located at $2\theta = 43.03^\circ$ and the 022 diffraction peak of fcc-Ni is at $2\theta = 51.85^\circ$. Thus, we attribute the phenomenon of the 2θ peak locations of $\text{Mn}_2\text{Ni}_2\text{N}$ as similar to that for Ni nitrides, which tend to easily denitride; and thus enhanced migration of N atoms is expected with high T_S in the $\text{Fe}_{4-x}\text{Ni}_x\text{N}$ thin films [20]. To mitigate this phenomenon, we grew the $x = 2$ samples at $T_S = 150$ °C, whereupon less decomposition occurred, as observed via XRD. However, the in-plane XRD peaks of these samples were asymmetric and broadened as 2θ increased, which we attributed to poor orientation and partial decomposition of the crystal. In particular, the diffraction peak from Ni_8N is obvious in the Ni_4N in-plane XRD pattern, which demonstrates the presence of an intermediate product between Ni_4N and fcc-Ni. The 100 or 001

diffraction peak of $\text{Mn}_{4-x}\text{Ni}_x\text{N}$ were superlattice lines emerging via the occupation of N atoms at the body-centered sites in the crystalline structure. These peaks also correspond to the lines indicated by arrows in the Fig. 2 RHEED patterns. When the value of x is not 0 or 4, the intensity of these diffraction peaks reduce and the N superlattice diffraction lines correspondingly become weak and vague.

Figure 4 plots the lattice constants (a , c) as a function of the Ni ratio x . At $x = 2$, these values could not be calculated because the diffraction peaks were not detectable. For the Mn-rich samples where $0 \leq x \leq 0.5$, the values of a and c were similar and corresponded well with the theoretical lattice constants of Mn_4N [19]. The ratios of the lattice constants were $c/a < 1$ for samples except $x = 3$, signifying in-plane tensile strains. The values of the lattice constants as a function of x largely follow Vegard's law in whole. However, in the Mn-rich $\text{Mn}_{4-x}\text{Ni}_x\text{N}$ samples ($0 \leq x \leq 0.5$), the values of c and a gradually increased with x even though the atomic radii of Ni ($r_{\text{Ni}} = 1.15 \text{ \AA}$) is smaller than that of Mn ($r_{\text{Mn}} = 1.17 \text{ \AA}$). The origin of this abnormal behavior and the tensile strain is under investigation. Several factors such as lattice mismatch and difference in thermal expansion coefficient between MgO and grown films should be considered; however, we do not have enough data to discuss with further at present.

Figure 5 shows the full width at half maximum of the in-plane XRD 002 peak (FWHM(002)) as a function of the Ni ratio x . A larger FWHM of the diffraction peak suggests a poorer crystal orientation, showing that the crystal orientation tended to degrade when the Ni composition was higher. We posit two explanations for this. The first is that the differing atomic radii of Mn and Ni distorted the structure from a perfect cubic or tetragonal structure as more Mn atoms were substituted with Ni atoms. Secondly, because T_s was set at $450 \text{ }^\circ\text{C}$ for $x \leq 1$ and at $150 \text{ }^\circ\text{C}$ for $x \geq 2$, where the latter was to avoid denitridation via the thermal energy from high T_s , the growth

conditions varied according to x . It is empirically known that the FWHM of a diffraction peak in XRD patterns, which indicates the crystalline orientation, depends on the growth temperature of the crystal including the nitrides, and each type of crystal has an ideal T_s for high crystalline orientation [20]. We assumed that a higher T_s was necessary for the improvement of crystal orientation. However, as mentioned above, this could cause increased structural decomposition of the structure and a reduced purity of the $\text{Mn}_{4-x}\text{Ni}_x\text{N}$. Further, a more detailed study of the effect of the variation of T_s will be needed to optimize the growth condition especially for $x > 1$. Regarding the position of Ni atoms, recent experiments using x-ray magnetic circular dichroism (XMCD) demonstrated that the Ni atoms in Fe_3NiN tend to occupy the I sites [29]. Therefore we speculate that the Ni atoms are likely to occupy the I sites in $\text{Mn}_{4-x}\text{Ni}_x\text{N}$ ($x \leq 1$).

As discussed above, it is difficult to exclude the influence of other phases such as fcc-Ni. Hence we focus our discussion on the magnetic properties of $\text{Mn}_{4-x}\text{Ni}_x\text{N}$ for $x \leq 1$. Figure 6 plots the magnetization vs. magnetic field ($M-H$) curves of $\text{Mn}_{4-x}\text{Ni}_x\text{N}$ ($x = 0, 0.1, 0.25, 0.5, 0.75, 1$) as measured by VSM at RT, and Fig. 7 plots the value of M_s and K_u of $\text{Mn}_{4-x}\text{Ni}_x\text{N}$ as a function of x . The field H was applied in the range of $-17-17$ kOe and in the directions parallel ([100]) and perpendicular ([001]) to the plane. In Fig. 6, the diamagnetic component has already been extracted. A small amount of Ni substitution of the Mn atoms drastically decreased the M_s value. For example, although the M_s of $x = 0$ was 86.3 ± 1.1 emu/cm³ (Mn_4N), it was almost quartered for $x = 0.1$ (24.2 ± 0.7 emu/cm³), and further decreased for $x = 0.25$ (19.0 ± 0.5 emu/cm³). When the shape of the $M-H$ loops in Fig. 6 were examined, it is clear that the Mn_4N exhibited a sharp magnetization reversal. However, the mixed crystals arising for $x = 0.1$ or 0.25 exhibited a remarkably smooth reversal. In addition, we can conclude that $\text{Mn}_{4-x}\text{Ni}_x\text{N}$ possesses PMA when $0 \leq x \leq 0.25$ by examining the $M-H$ curves. The values of K_u was

approximately 0.94 Merg/cm^3 at $x = 0$, and decreased sharply to 0.027 Merg/cm^3 at $x = 0.25$. Magnetic anisotropy was scarcely observed when $x \geq 0.5$, and the samples exhibited paramagnetic behavior for higher x values. Considering its potential application in a domain wall motion device, we believe that further studies of the properties of $\text{Mn}_{4-x}\text{Ni}_x\text{N}$, and especially for $0 \leq x \leq 0.25$ where small M_S and measurable PMA were observed, are important.

4. Conclusion

We successfully grew $\text{Mn}_{4-x}\text{Ni}_x\text{N}$ epitaxial thin films on $\text{MgO}(001)$ by MBE and subsequently measured their magnetic properties. It was found via XRD and RHEED patterns that the films were significantly decomposed into Ni_8N or Mn-Ni alloys when $x \geq 2$, but this decomposition was mitigated when T_S was set at $150 \text{ }^\circ\text{C}$. The lattice constants reduced with increasing Ni ratio in a trend that followed Vegard's law except when the Mn ratio was high. The crystal orientation tended to degrade as the Ni ratio increased, which we attributed to the distorted structure in the film and difference in T_S in the growth process. We examined the magnetic properties of the films, and it was found that the M_S and PMA drastically decreased after a small amount of Ni substitution. For example, the M_S of Mn_4N was $86.3 \pm 1.1 \text{ emu/cm}^3$, while that of $\text{Mn}_{3.75}\text{Ni}_{0.25}\text{N}$ was $19.0 \pm 0.5 \text{ emu/cm}^3$. The magnetic anisotropy constant decreased sharply from approximately 0.94 Merg/cm^3 for Mn_4N to 0.027 Merg/cm^3 for $\text{Mn}_{3.75}\text{Ni}_{0.25}\text{N}$. According to the shape of the $M-H$ curves, PMA was observed when $0 \leq x \leq 0.25$.

Acknowledgments

Magnetization measurements were performed with the help of Professor H.

Yanagihara from the University of Tsukuba. T.G. was financially supported by a Grant-in-Aid for JSPS Fellows (No. 16J02879).

Figure captions

Figure 1 Antiperovskite structure of Mn_4N . The face-centered II sites can be further divided into IIA and IIB sites under the presence of an external magnetic field denoted by arrow.

Figure 2 Out-of-plane XRD (line spectra) and RHEED (inset images) patterns along the $\text{MgO}[100]$ azimuth of $\text{Mn}_{4-x}\text{Ni}_x\text{N}$ for $x=0, 0.1, 0.25, 0.5, 0.75, 1, 2, 3$ and 4. The white arrows in the insets indicate the position of superlattice diffraction lines. The substrate growth temperature T_S was 450°C for $x \leq 2$ and 150°C for $2 \leq x \leq 4$.

Figure 3 In-plane XRD patterns of $\text{Mn}_{4-x}\text{Ni}_x\text{N}$ for $x=0, 0.1, 0.25, 0.5, 0.75, 1, 2, 3$ and 4. The scattering vector was set along $\text{MgO}[100]$. The substrate growth temperature T_S was 450°C for $0 \leq x \leq 2$ and 150°C for $2 \leq x \leq 4$.

Figure 4 In-plane lattice constant a (closed circles) and out-of-plane lattice constant c (open squares) of $\text{Mn}_{4-x}\text{Ni}_x\text{N}$ as a function of x .

Figure 5 FWHM of the in-plane XRD peak for $\text{Mn}_{4-x}\text{Ni}_x\text{N}$ as a function of x .

Figure 6 Magnetization vs. magnetic field ($M-H$) curves of $\text{Mn}_{4-x}\text{Ni}_x\text{N}$ measured at RT. Blue (red dotted) line indicates the data perpendicular (parallel) to the sample surface, $\text{Mn}_{4-x}\text{Ni}_x\text{N}[001]$ ($\text{Mn}_{4-x}\text{Ni}_x\text{N}[100]$).

Figure 7 Saturation magnetization (M_S) (closed circles) and magnetic anisotropy constant (K_u) (open squares) of $\text{Mn}_{4-x}\text{Ni}_x\text{N}$ as a function of x .

Reference

- [1] S. S. P. Parkin, M. Hayashi, L. Thomas, *Science* 320 (2008) 190.
- [2] S. Fukami, T. Suzuki, K. Nagahara, N. Ohshima, Y. Ozaki, S. Saito, R. Nebashi, N. Sakimura, H. Honjo, K. Mori, C. Igarashi, S. Miura, N. Ishiwata and T. Sugibayashi, 2009 Symposium on VLSI Technology. Digest Tech. Pap. (2009) 230.
- [3] I. M. Miron, T. Moore, H. Szabolcs, L. D. Buda-Prejbeanu, Stéphane Auffret, B. Rodmacq, S. Pizzini, J. Vogel, M. Bonfim, A. Schuhl, G. Gaudin, *Nature Mater.* 10 (2011) 419.
- [4] A. J. Schellekens, A. van den Brink, J.H. Franken, J.J.M. Swagten, B. Koopmans, *Nature Commun.* 3 (2012) 847.
- [5] K. M. Ching, W. D. Chang, T. S. Chin, *J. Alloys Compd.* 222 (1995) 184.
- [6] K. M. Ching, W. D. Chang, T. S. Chin, J. G. Duh, H. C. Ku, *J. Alloys Compd.* 76 (1994) 6582.
- [7] D. Dhar, O. Brandt, and H. Ploog, *Appl. Phys. Lett.* 86 (2005) 112504.
- [8] M. Tsunoda and K. Kabara, International Conference of the Asian Union of Magnetism Societies (ICAUMS) 2pPS-47, Nara, Japan, Oct. 2, 2012.
- [9] Y. Yasutomi, K. Ito, T. Sanai, K. Toko, T. Suemasu, *J. Appl. Phys.* 115 (2014) 17A935.
- [10] X. Shen, A. Chikamatsu, K. Shigematsu, Y. Hirose, T. Fukumura, T. Hasegawa, *Appl. Phys. Lett.* 105 (2014) 072410.
- [11] M. Meng, S. X. Wu, L. Z. Ren, W. Q. Zhou, Y. J. Wang, G. L. Wang, S. W. Li, *Appl. Phys. Lett.* 106 (2015) 032407.
- [12] K. Kabara, M. Tsunoda, *J. Appl. Phys.* 117 (2015) 17B512.
- [13] A. Anzai, F. Takata, T. Gushi, K. Toko, T. Suemasu, *J. Cryst. Growth* 489 (2018) 20.
- [14] K. Ito, Y. Yasutomi, K. Kabara, T. Gushi, S. Higashikozono, K. Toko, M. Tsunoda, T. Suemasu, *AIP Adv.* 6 (2016) 056201.
- [15] T. Gushi, L. Vila, J. P. Attané, O. Fruchart, A. Marty, S. Pizzini, J. Vogel, M. Klug, J. Pena-Garcia, A. Anzai, T. Komori, T. Suemasu, *Jpn. Soc. Appl. Phys. Fall Meeting*, 18a-131-6, Nagoya, Japan, Sept. 18 (2018).
- [16] W. J. Takei, R. R. Heikes, G. Shirane, *Phys. Rev.* 125 (1962) 1893.
- [17] G. J. W. Dorman, M. Shikkens, *Thin Solid Films* 105 (1983) 251.
- [18] M. Markus, *J. Phys. Condens. Matter* 28 (2016) 056006.
- [19] N. Terano, *J. Phys. Soc. Jpn.* 15 (1960) 227.
- [20] F. Takata, K. Ito, S. Higashikozono, T. Gushi, K. Toko, T. Suemasu, *J. Appl. Phys.* 120 (2016) 083907.
- [21] K. Ito, T. Sanai, Y. Yasutomi, S. Zhu, K. Toko, Y. Takeda, Y. Saitoh, A. Kimura, T. Suemasu, *J. Appl. Phys.* 115 (2014) 17C712.
- [22] Y. Na, C. Wang, E. Tomasella, J. Cellier, J. Xiang, *J. Alloys Compd.* 647 (2015) 35.
- [23] T. Shibayama, K. Takenaka, *J. Appl. Phys.* 109 (2011) 07A928.

- [24] K. Takenaka, T. Shibayama, K. Asano, K. Koyama *J. Phys. Soc. Jpn.* 79 (2010) 073706.
- [25] D. Boldrin, L. F. Cohen, *J. Alloys. Compd.* 699 (2017) 887.
- [26] E. V. Gomonaj, *Phase Transitions* 18 (1989) 93.
- [27] E. V. Gomonaj, V. A. Lvov, *J. Magn. Magn. Mater.* 86 (1990) 301.
- [28] S. Deng, Y. Sun, H. Wu, Q. Huang, J. Yan, K. Shi, M. I. Malik, H. Lu, L. Wang, R. Huang, L. Li, C. Wang, *Chem. Mater.* 27 (2015) 2495
- [29] F. Takata, K. Ito, Y. Takeda, Y. Saitoh, K. Takanashi, A. Kimura, T. Suemasu, *Phys. Rev. Mater.* 2 (2018) 024407.

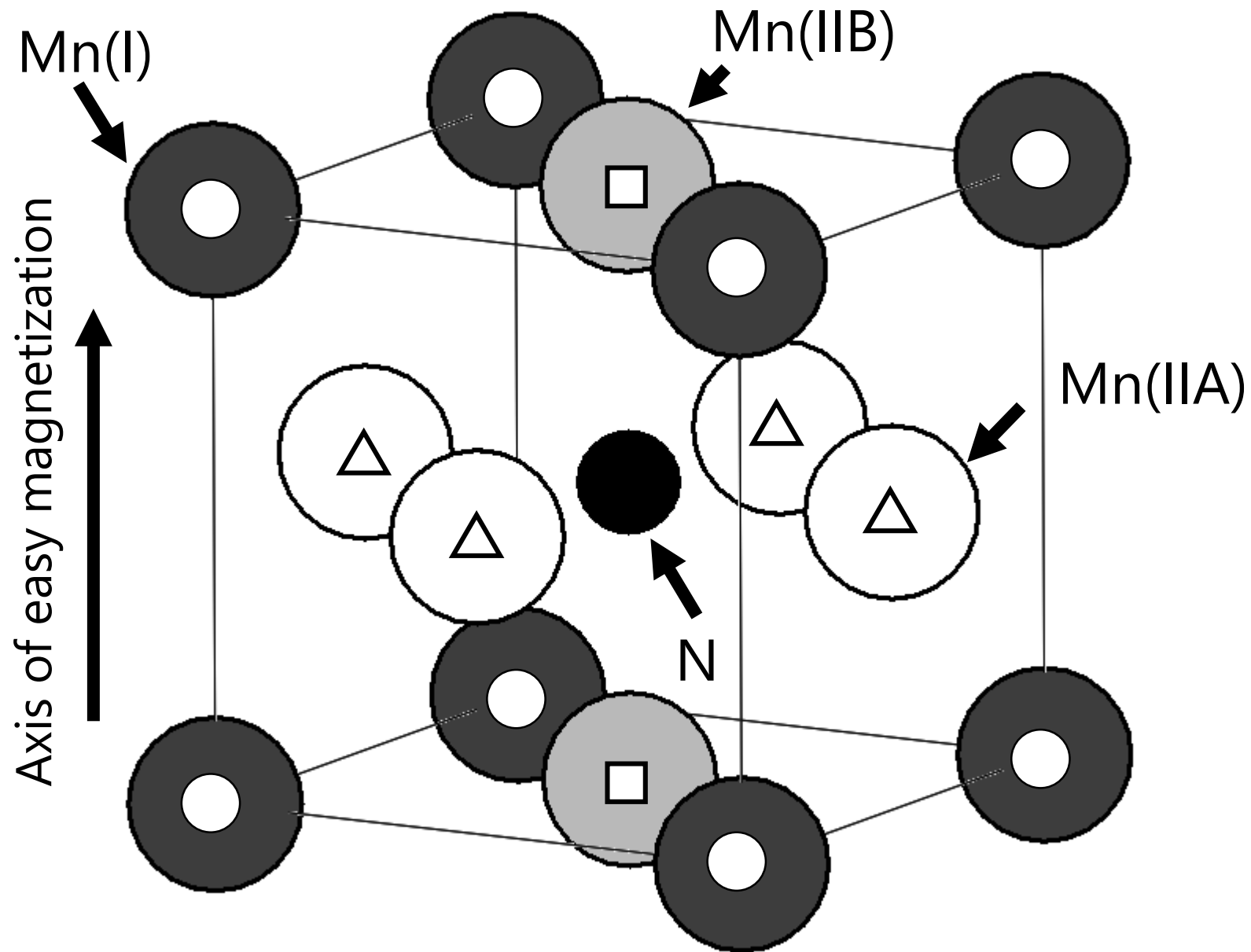


Fig. 1

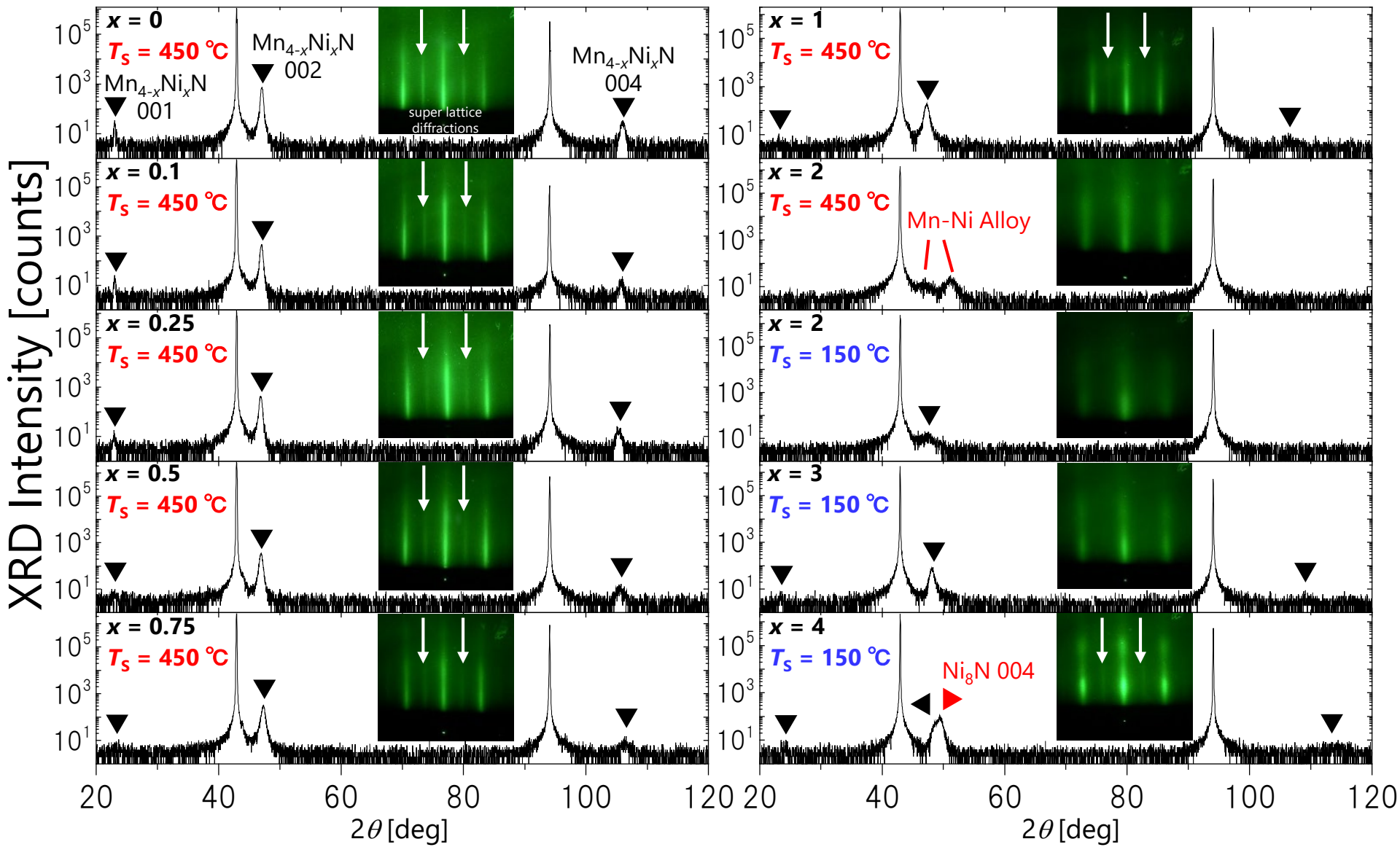


Fig. 2

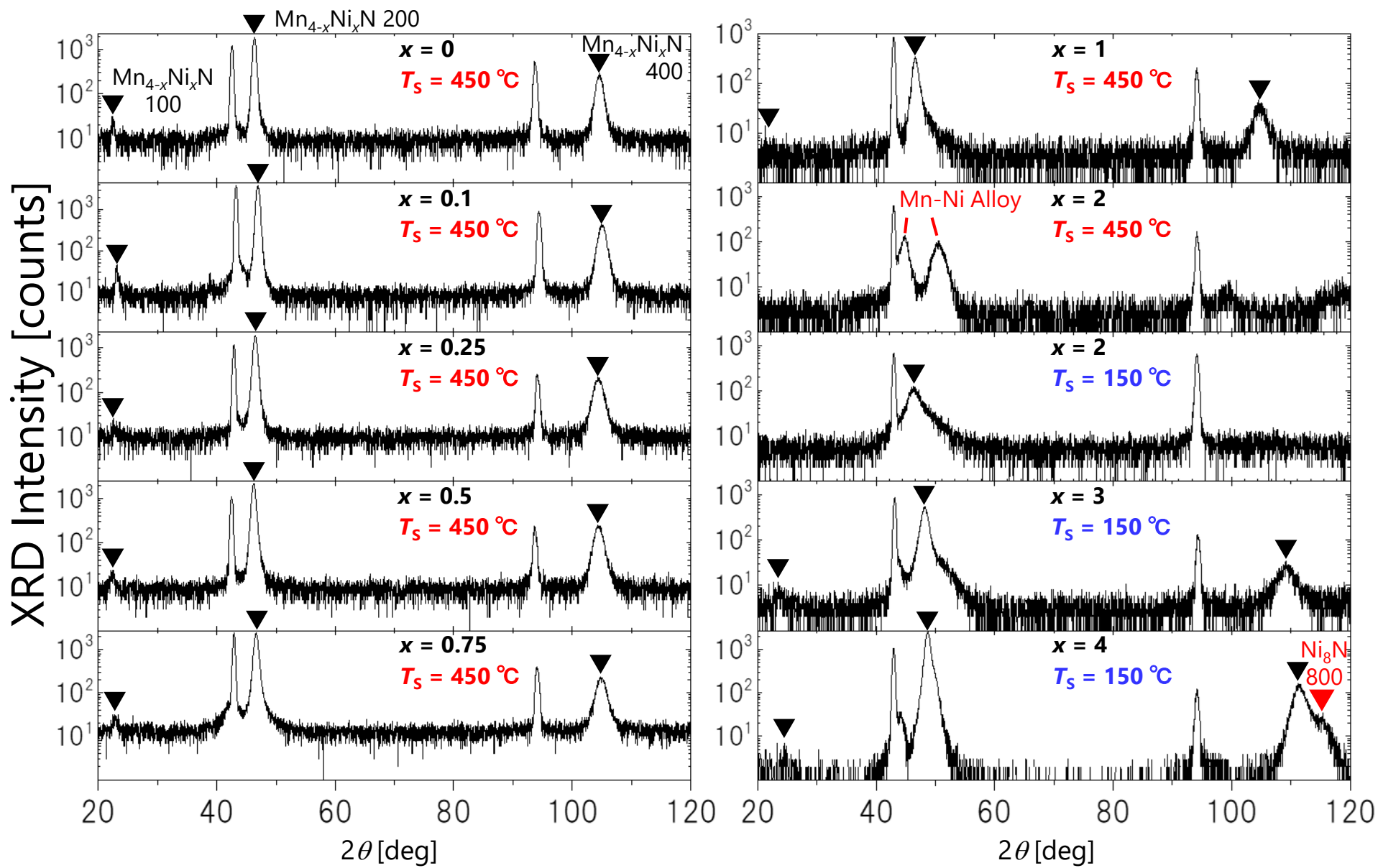


Fig. 3

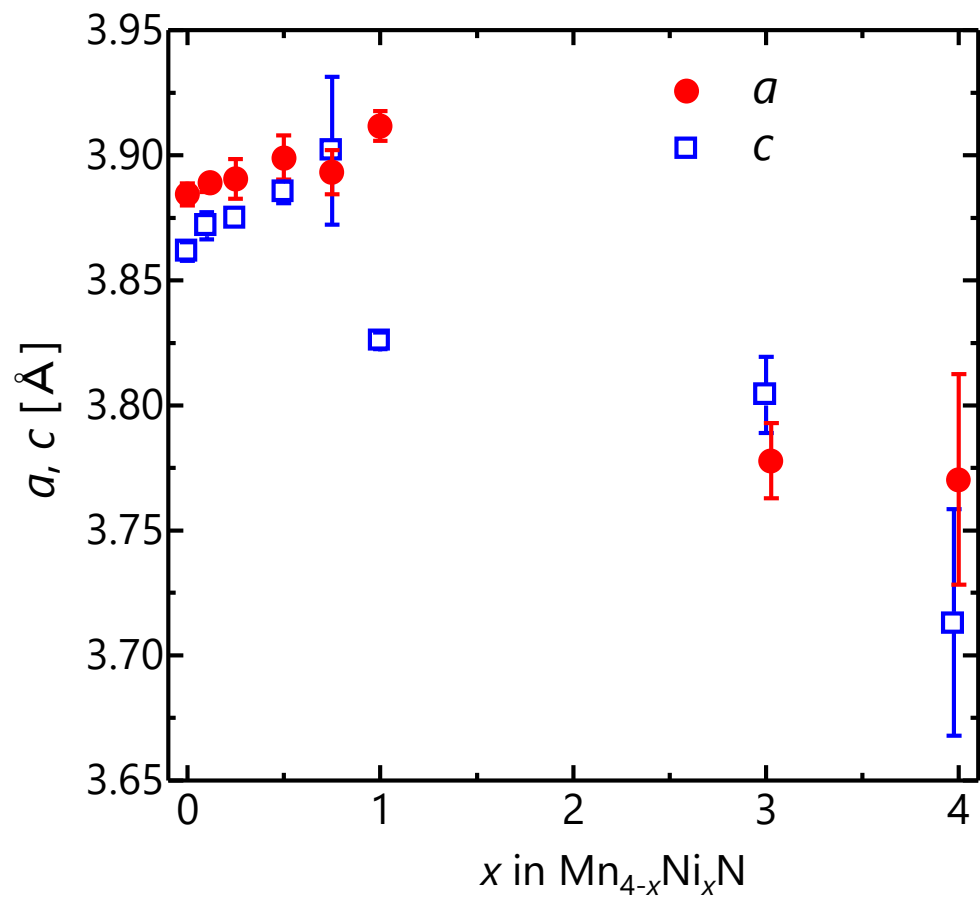


Fig. 4

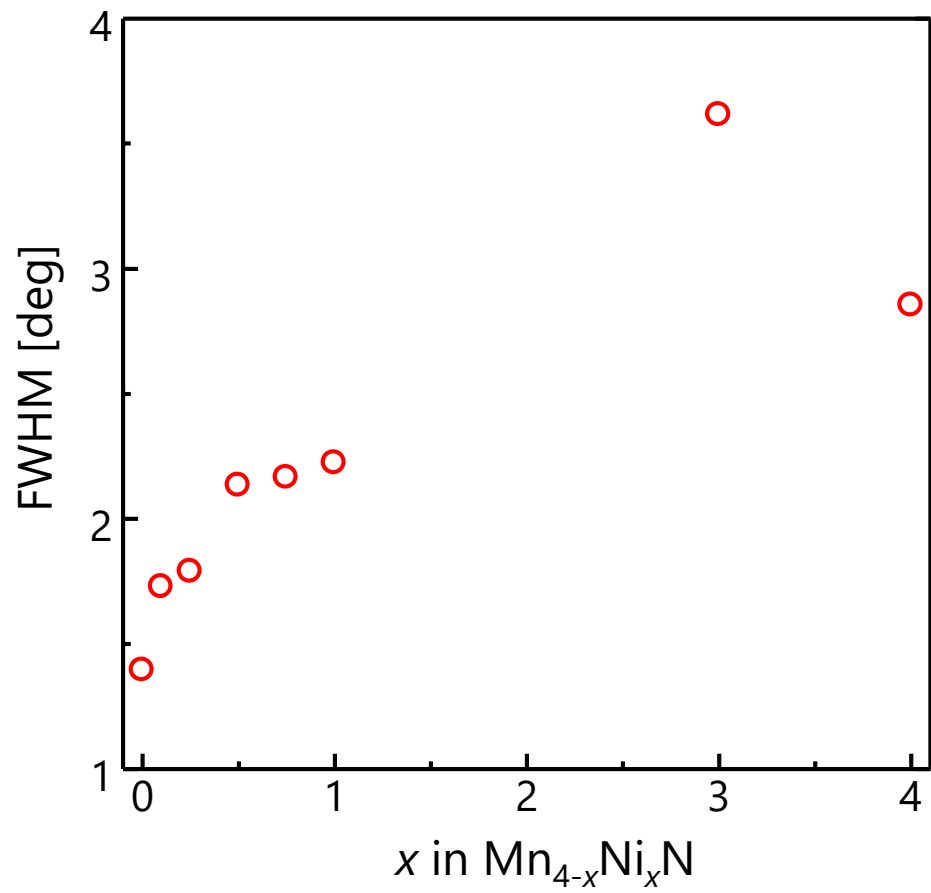


Fig. 5

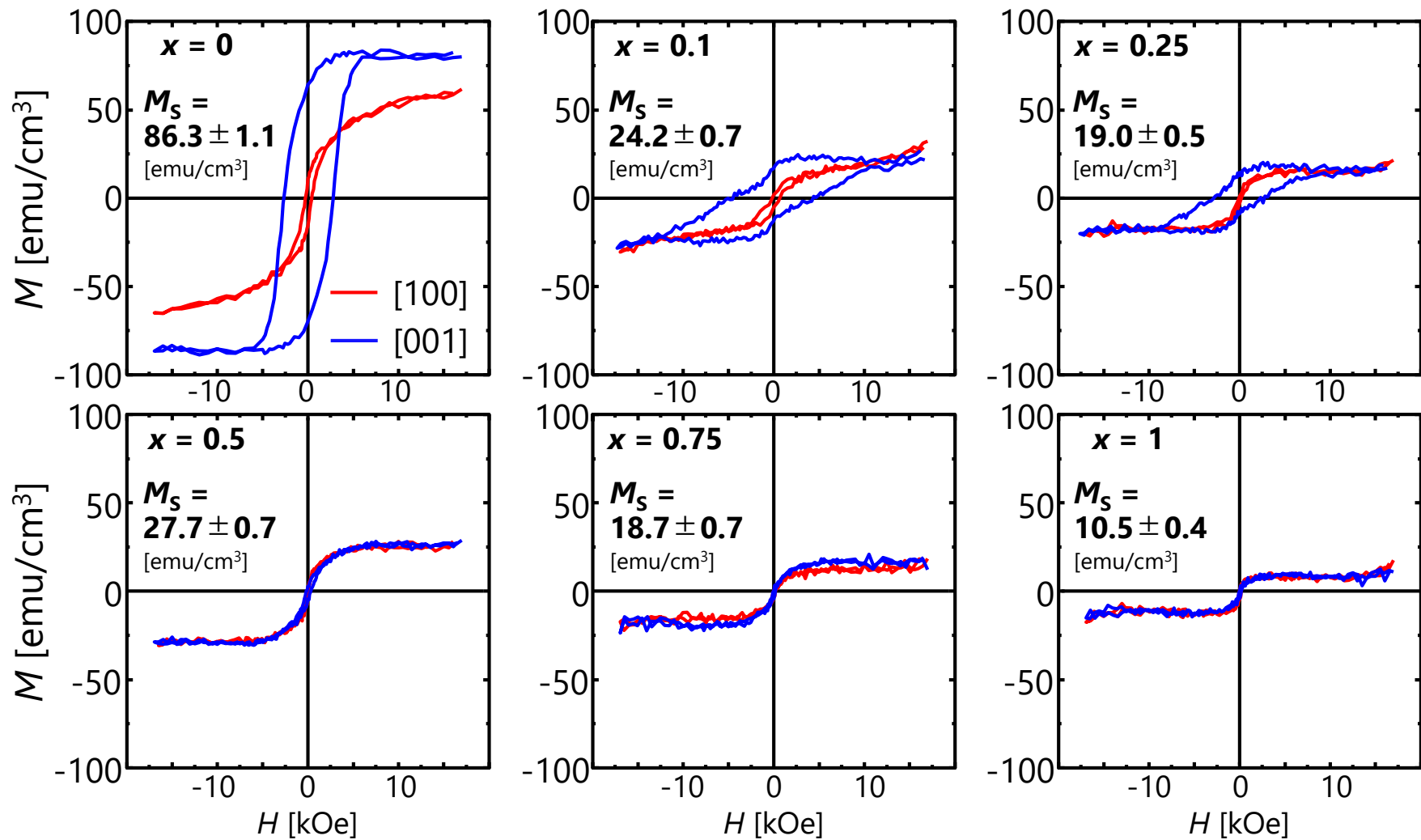


Fig. 6

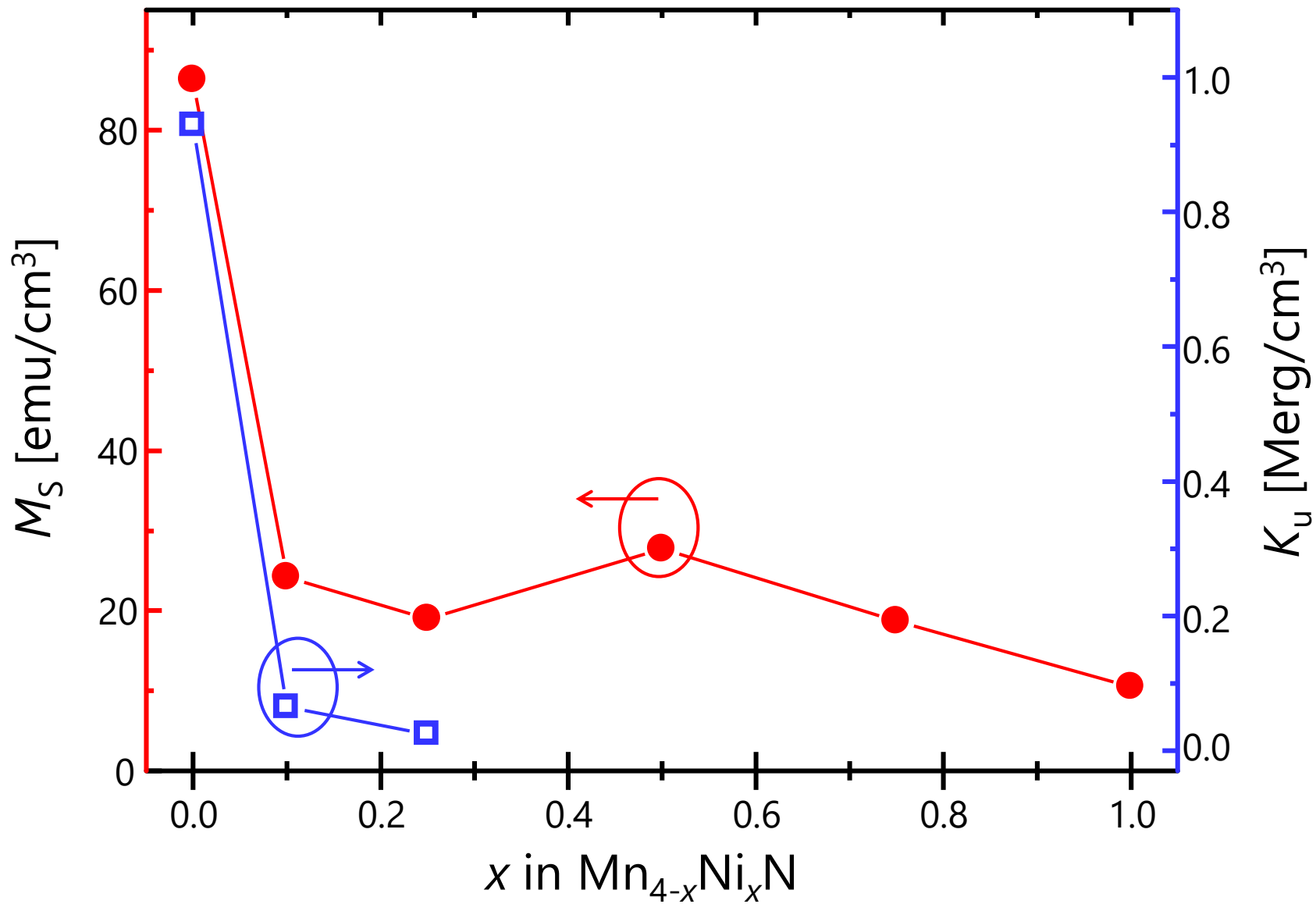


Fig. 7